An organic transistor matrix for multipoint intracellular action potential recording

Yasutoshi Jimbo[a], Daisuke Sasaki[b], Takashi Ohya[c], Sunghoon Lee[a], Wonryung Lee[a,1], Faezeh Arab Hassani[a,2], Tomoyuki Yokota[a], Katsuhisa Matsuura[b], Shinjiro Umezu[c], Tatsuya Shimizu[b], and Takao Someya[a,3]

[a]Department of Electrical Engineering and Information Systems, Graduate School of Engineering, The University of Tokyo, Tokyo 113-8656, Japan; [b]Institute of Advanced Biomedical Engineering and Science, Tokyo Women's Medical University, Tokyo 162-8666, Japan; and [c]Graduate School of Creative Science and Engineering, Waseda University, Tokyo 169-8555, Japan

Edited by John A. Rogers, Northwestern University, Evanston, IL, and approved August 11, 2021 (received for review October 25, 2020)

Electrode arrays are widely used for multipoint recording of electrophysiological activities, and organic electronics have been utilized to achieve both high performance and biocompatibility. However, extracellular electrode arrays record the field potential instead of the membrane potential itself, resulting in the loss of information and signal amplitude. Although much effort has been dedicated to developing intracellular access methods, their three-dimensional structures and advanced protocols prohibited implementation with organic electronics. Here, we show an organic electrochemical transistor (OECT) matrix for the intracellular action potential recording. The driving voltage of sensor matrix simultaneously causes electroporation so that intracellular action potentials are recorded with simple equipment. The amplitude of the recorded peaks was larger than that of an extracellular field potential recording, and it was further enhanced by tuning the driving voltage and geometry of OECTs. The capability of miniaturization and multiplexed recording was demonstrated through a 4 × 4 action potential mapping using a matrix of 5- × 5-μm^2 OECTs. Those features are realized using a mild fabrication process and a simple circuit without limiting the potential applications of functional organic electronics.

organic electronics | organic electrochemical transistor | intracellular recording | action potential mapping | biomonitoring interface

Organic electronics offer high performance and biocompatibility to next-generation bioelectronic interfaces by taking advantage of the diversity of organic materials (1–4). In particular, for in vitro electrogenic cell monitoring, flexible, soft, and porous materials have been utilized for three-dimensional monitoring and for the suppression of mechanical perturbation (3, 5–7). In this platform, organic transistors have been employed to record activities with a high signal-to-noise ratio (SNR), owing to their high input impedance and amplification (8, 9). Organic electrochemical transistors (OECTs), which use a mixed ion-electron conductor such as poly(3,4-ethylenedioxythiophene):poly(styrenesulfonate) (PEDOT:PSS) as a channel material, achieve a high current and transconductance (g_m) (10–12). Therefore, heat generation is suppressed and the area occupied by interdigitated electrode is reduced, even for high-resolution recording on small tissues. The fabrication on a soft substrate (13, 14) and multipoint field potential recording with a common-source array configuration (15, 16) have been reported.

Most of the sensor arrays, which are designed for action potential mapping, record field potential through an extracellular contact. On the other hand, direct membrane potential recording through intracellular access has a larger amplitude and thus achieves a high SNR recording (17, 18). Furthermore, additional information such as the action potential duration can be evaluated based on the low-frequency components that are not included in the field potential. That information can be utilized for testing drug efficacy and side effects (19, 20). The patch-clamp method is widely used as an established way to gain intracellular access reproducibly (21). Toward large-scale recording, three-dimensional nanostructures (17, 18, 20, 22–24), biomimetic materials (17), and membrane poration and permeabilization methods (18, 20, 23, 25, 26) have been developed to attain multipoint intracellular access. Recently, the combination of those techniques and the silicon (Si) microfabrication platform demonstrated the parallel recording from more than 1,000 points (20, 23).

However, intracellular action potential recording utilizing organic transistor has not been demonstrated yet. Soft organic materials are not suitable to form a needle-like, three-dimensional nanostructure that penetrates cells. In the case of typical recording using OECT, the interface with cells is a flat PEDOT:PSS film and array is driven by direct current (DC) drain bias. Thus, it does not have any intracellular access and records the field potential as extracellular electrodes do.

Here, we demonstrate an intracellular action potential recording by an organic transistor. The feasibility of multipoint intracellular action potential recording is confirmed by a parallel recording with a 4 × 4 matrix. In a matrix configuration, the line-by-line application of a pulse bias to the drain electrode causes on-channel electroporation, leading to intracellular access. Therefore, multipoint intracellular access is obtained using simple equipment that has been used for field potential recording so far. The effect of electroporation can be controlled by

Significance

We successfully performed the intracellular action potential recording using organic electrochemical transistors (OECTs). A simultaneous multipoint recording with a 4 × 4 matrix of 5- × 5-μm^2 OECTs demonstrated the feasibility of potential high-resolution recording. The intracellular access was obtained by applying a pulse voltage to the drain electrode, and the amplitude of recorded signal reached 93 μA at maximum. This simple intracellular access method offers a higher signal-to-noise ratio and the waveform of membrane potential compared to the conventional extracellular field potential recording by OECT arrays.

Author contributions: Y.J. and T. Someya designed research; Y.J., D.S., and T.O. performed research; Y.J. contributed new reagents/analytic tools; Y.J., D.S., S.L., W.L., F.A.H., T.Y., K.M., S.U., T. Shimizu, and T. Someya analyzed data; and Y.J. and T. Someya wrote the paper.

Competing interest statement: T. Shimizu and K.M. are inventors of the bioreactor system for differentiation culture of pluripotent stem cells, the patents of which are held by Able Co. and Tokyo Women's Medical University.

This article is a PNAS Direct Submission.

[1]Present address: Biomedical Research Institute, Korea Institute of Science and Technology, Seoul 02792, Republic of Korea.

[2]Present address: Department of Electrical and Electronic Engineering, University of Bristol, BS8 1UB Bristol, United Kingdom.

[3]To whom correspondence may be addressed. Email: someya@ee.t.u-tokyo.ac.jp.

This article contains supporting information online at https://www.pnas.org/lookup/suppl/doi:10.1073/pnas.2022300118/-/DCSupplemental.

Published September 20, 2021.

tuning the geometry and driving the voltage of OECTs, and thus intracellular action potential and field potential can be selectively recorded.

Working Principle of the OECT Matrix

Fig. 1*A* presents a 4 × 4 OECT matrix. The scan lines are turned on one by one, and all four sensors on one scan line are simultaneously read out through data lines. A conventional electrode array or OECT common-source array has approximately N × M of wires for N × M arrays. This matrix configuration reduces the number of wires to approximately N + M. Thus, multipoint recording can be performed with less readout equipment, and spatial resolution can be potentially increased. Human-induced pluripotent stem cell–derived (hiPSC-derived) cardiomyocytes were cultured directly on the OECT matrix. Its surface was coated with fibronectin to enhance cell adhesion. As shown in Fig. 1*B*, the cells cover the entire surface and are clearly observed on the transparent PEDOT:PSS channel (the scanning electron microscopy image is shown in *SI Appendix*, Fig. S1). Recordings were performed using the configuration shown in Fig. 1*C*. The drain current flows from one Au electrode to the other through the PEDOT:PSS channel. The electrical potential generated by the cells injects ions from the electrolyte into the PEDOT:PSS channel, and the conductivity of PEDOT:PSS is then suppressed by the dedoping process (27). This depletion in drain current represents the readout signal. The culture medium works as an electrolyte gate, and another PEDOT:PSS/Au electrode immersed in the medium works as a reference electrode.

A recorder and power supply for the drain-source bias voltage are connected externally. By switching the supplied voltage from DC to pulse, we intend to selectively measure the field potential and intracellular action potential (Fig. 1 *D* and *E*). When a DC drain-source bias is applied, almost no current flows between the drain and the reference electrode. Thus, the extracellular field potential is recorded on the baseline of the drain-source current. However, when a pulse drain-source bias is applied, the high-frequency component leaks from the drain to the reference electrode along with each rise and fall of the pulse. This means that a large electrical field is applied to the membrane, which causes electroporation, and the recorded signals demonstrate the intracellular action potential feature. Furthermore, when an OECT is driven in a matrix, the pixels are switched on/off by a pulse input to the scan lines. Therefore, the intracellular action potential can be recorded at multiple points without adding the special function of stimulation to the recording systems.

Characteristics of OECTs

The electrical performance of OECTs was confirmed before in vitro recording. For these characterizations, an Ag/AgCl electrode was used as the gate electrode. The width, length, and thickness of the PEDOT:PSS channel were 25 μm, 25 μm, and 100 nm, respectively. Fig. 2*A* illustrates the relationship between the gate voltage and drain current of an OECT. The g_m of the OECT reached ∼2 mS at gate voltage of 0 V. This value is consistent with a typical performance of a PEDOT:PSS OECT (11). Fig. 2*B* shows the time response of the drain current when a 100-mV rectangular wave is applied to the gate. The response time as a time constant of the exponential fitting to the transient current was 62 μs. This response time is sufficiently short to record an action potential and can be tuned faster by changing the geometries of the channel (11). Both a culture medium and saline solution were used as electrolytes and the performance was compared, but there was no difference except for the baseline shift. Fig. 2*C* shows the drain current and gate current when a pulse of −600 mV is applied to the drain electrode. The high-frequency component flows from the drain electrode to the gate electrode through the channel following the rise of pulse. It means an electric field is applied to the cells on channel and possibly causes electroporation.

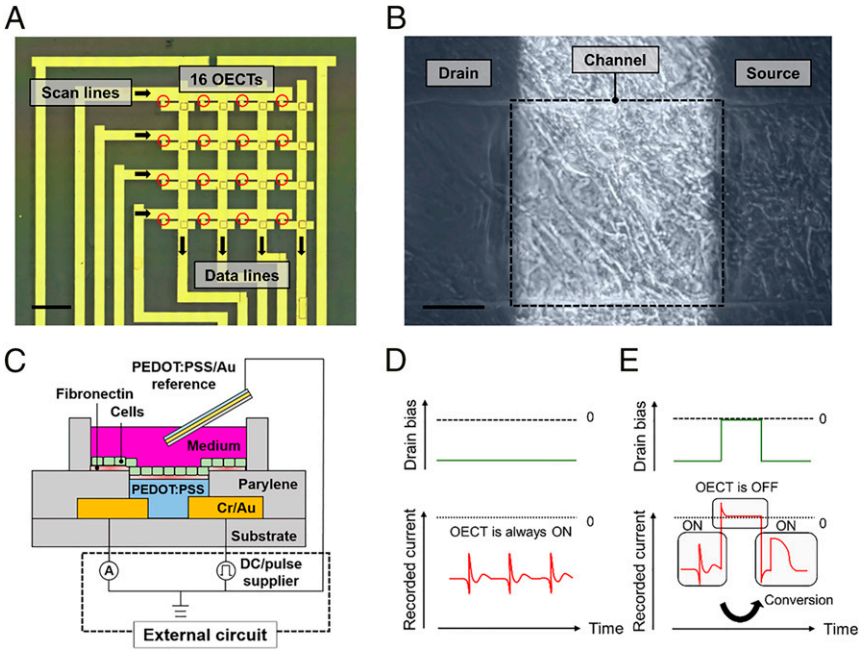

Fig. 1. Concept of intracellular action potential recording using an OECT matrix supported by electroporation. (*A*) Top-view photograph of a 4 × 4 OECT matrix generated by merging microscopic images. Each channel (size: 5 × 5 μm^2, red circle) is placed at a 2-mm spacing. The outer line is a sample for a test run. (Scale bar, 2 mm.) (*B*) hiPSC cardiomyocytes cultivated on a channel (size: 300 × 300 μm^2). (Scale bar, 100 μm.) (*C*) Schematic illustration of the structure and circuit configuration of an OECT where cells are cultured. (*D* and *E*) Illustration of the signals recorded by OECT supplied with a DC drain voltage (*D*) and pulse drain voltage (*E*). On applying a pulse drain voltage, a high-frequency component flows from the drain to the reference electrode causing electroporation, and thus the intracellular action potential is recorded.

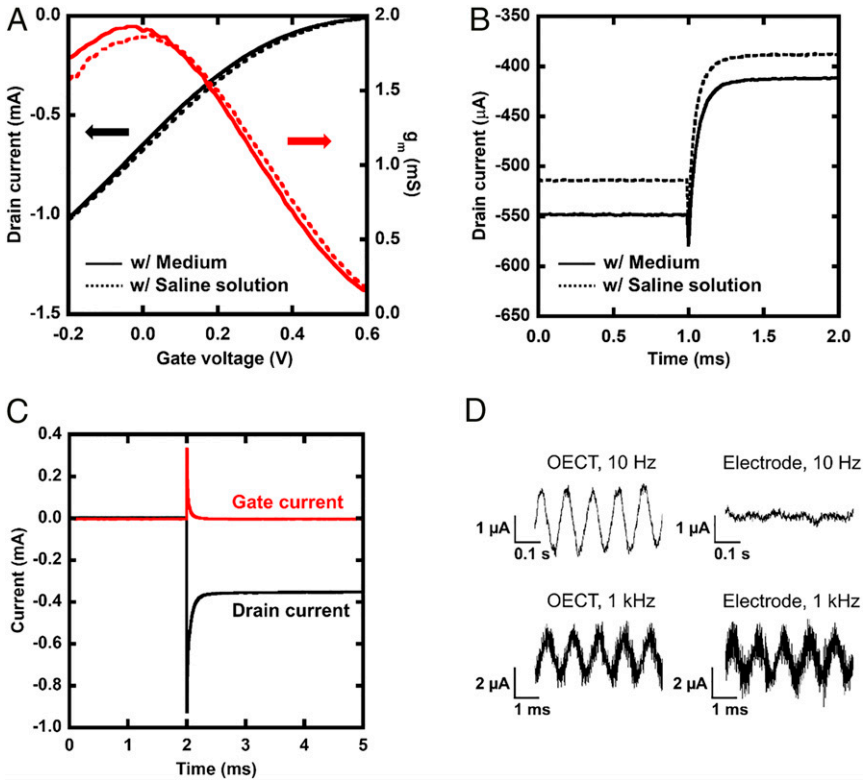

Fig. 2. Electrical performance of an OECT. (*A*) Gate voltage versus drain current and g_m. The solid black line indicates the drain current when the medium is put on the channel as an electrolyte, the dotted black line indicates the drain current with the saline solution, the solid red line indicates g_m with the medium, and the dotted red line indicates g_m with the saline solution. (*B*) Time response of the drain current when a 100-mV pulse was input to the gate electrode since 1 ms. The OECTs on which the medium and saline solution was placed as an electrolyte were compared. (*C*) Transient response of a drain and gate current when a pulse voltage (−600 mV) was input to the drain electrode since 2 ms. A spike was observed immediately after the pulse was applied. (*D*) Comparison of recorded data when a 2-mV peak-to-peak sine wave is applied to an OECT and a PEDOT:PSS electrode.

The amplitude of a recorded signal is strongly affected by the electrical performance of the sensing elements. Fig. 2*D* presents the output current recorded by an OECT and a PEDOT:PSS electrode of the same size under sine-wave input. When a 1-kHz sine wave was applied, both the OECT and PEDOT:PSS electrodes were capable of recording. However, only the OECT successfully recorded a 10-Hz sine wave. The impedance of the electrode and g_m of OECTs are major factors that determine the input voltage–output current characteristics. We measured the frequency response of them and compared in *SI Appendix*, Fig. S2. The OECT has a cutoff frequency at ∼1.1 kHz, and the response attenuates at frequencies above this value. On the other hand, the PEDOT:PSS electrode has a very low admittance in the low-frequency region. At frequencies below 1 kHz, the g_m of the OECT is greater than the admittance of the PEDOT:PSS electrode. Thus, we can expect a larger output signal amplitude by using OECTs for intracellular action potential recording. It should be noted that in a practical recording, signal quality is possibly affected by other factors such as input impedance of external circuits and the noise from a power source.

Electroporation and Recording Using OECT

We measured the extracellular field potential and electroporation-induced intracellular action potential of cardiomyocytes using a single-point OECT. Fig. 3*A* presents the conversion of the field potential recording into the intracellular action potential recording. During the first 5 s, the drain-source voltage was fixed at −600 mV DC, and the field potential was recorded (Fig. 3 *A*, *i*). Then, from 5 to 6 s, we applied a pulse drain-source voltage of 1,000 cycles. The voltage made round trips between 0 mV (0.25 ms) and −600 mV (0.75 ms), and currents flowed between the drain and reference electrodes. During the pulse input, the drain current reached a value lower than the baseline for the DC input due to an undershoot (a magnified figure of this part is presented in *SI Appendix*, Fig. S3). After the pulse input, the current quickly returned to the baseline, and the recorded signals demonstrated the effect of electroporation. Before the pulse input, the duration of a single peak was ∼5 ms (*SI Appendix*, Fig. S4), but after the pulse input, it had a longer duration, which was specific to the intracellular action potentials. The action potential duration at 50% of the maximum amplitude was 0.27 s. This electroporation-induced peak attenuated over several seconds to several tens of seconds, showing the phase overlapped with the field potential (Fig. 3 *A*, *ii*) and then returned to a waveform similar to the field potential (Fig. 3 *A*, *iii*).

Electroporation occurs when a pulse voltage that is larger than the threshold is applied, and the duration for returning to the original state increases as the voltage increases (25). Fig. 3*B* shows the recorded waveforms when the applied voltage was varied. When the amplitude of drain voltage and pulse voltage was 200 mV, no intracellular action potential was recorded. On increasing it to 400 mV, on the other hand, electroporation-induced peaks were observed, but they attenuated rapidly before the baseline returned. When the amplitude of input was increased to 600 mV, the amplitude of the recorded signal became larger and the effect of electroporation lasted longer.

The amplitude of the electroporation-induced peaks and its decay are plotted in Fig. 4*A*. Peaks are counted from the end of the pulse input, and the first peak is omitted because it is difficult to distinguish from the steep recovery of the baseline from undershoot

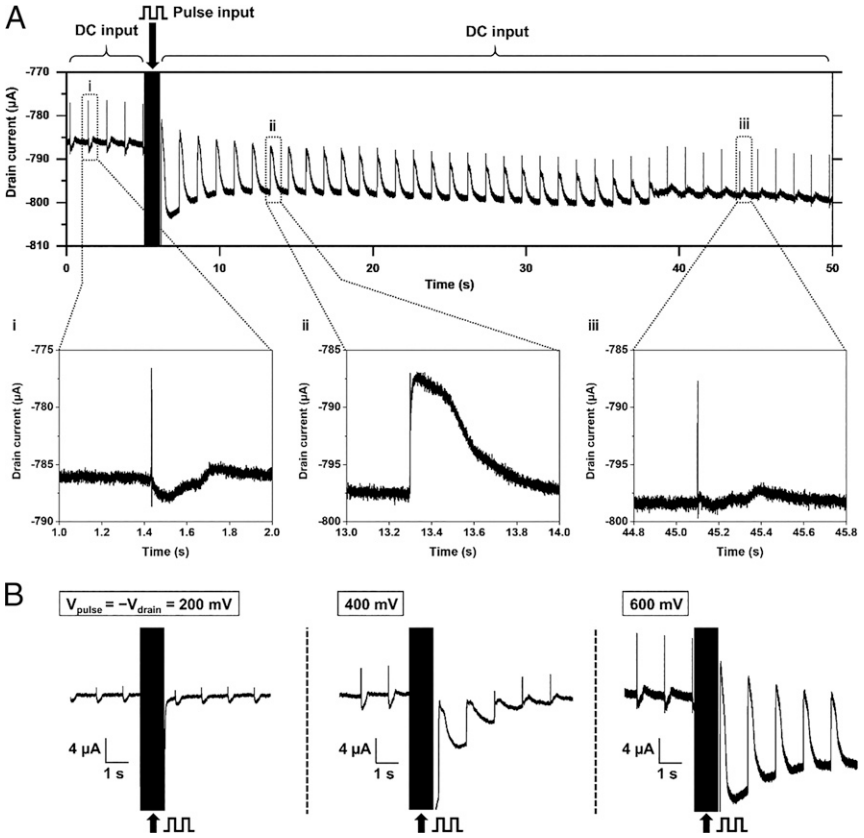

Fig. 3. Controlled intracellular action potential recording. (*A*) Sequential recording of field potentials and intracellular action potentials. Pulse drain voltage (1 kHz, −600 to 0 mV) was applied during 5 to 6 s. The shape of the peaks was converted by the pulse through this period and as time passed, it recovered itself. (*i*) Magnified signals before the pulse input, (*ii*) after the pulse input, and (*iii*) after the recovery. (*B*) Effect of the amplitude of the drain and pulse voltage. As it increases, the intracellular potential appeared and became larger.

(*SI Appendix*, Fig. S5). In addition, in order to exclude the influence of the amplification factor, which is highly dependent on the driving voltage, the peak current was normalized using the amplitude of the field potential that is recorded before the pulse input. Upon applying a 600-mV pulse, the amplitude of the electroporation-induced peak became larger than that of the field potential, and it lasted longer. Although the trend was consistent, the exact threshold voltage was dependent on each sample, and the electroporation-induced peak was occasionally induced by a 200-mV pulse (*SI Appendix*, Fig. S6). Fig. 4*B* shows the effect of the channel size when the pulse voltage is fixed at 600 mV. A smaller channel resulted in larger electroporation-induced peaks. In this scaling, the length of the overlap between the Au/PEDOT:PSS was fixed at 20 μm. The additional data of OECTs with a larger overlap size are also available in *SI Appendix*, Fig. S7.

When OECTs are driven in a matrix, the switching voltage works as pulse input, and the value of currents, while it is on, is recorded. In addition, based on the aforementioned trend, a larger amplitude of peaks is expected by simultaneously inducing electroporation during the recording. Therefore, extracting signals recorded while an OECT is on, which overlaps with the undershoot, is also important. The signals extracted by processing on software are presented in *SI Appendix*, Fig. S8. The sample with the smallest channel (100 × 100 μm^2) exhibited the largest electroporation-induced peak (93 μA). It is significantly larger than the field potential recorded by the same sample (1.8 μA). As shown in Fig. 4*C*, this method revealed that even for a 200-mV pulse, electroporation was induced temporally. The amplitude of the recorded signal was approximately five times larger than that of the extracellular field potential, and it recovered immediately to the initial state, thus minimizing the effect of electroporation on the cells. It should be noted that, although electroporation was induced, the interval of the peaks was maintained nearly constant before and after the pulse input under various conditions (*SI Appendix*, Table S1). Additionally, it was verified that electroporation did not affect the waveform of a field potential recorded 30 min later (*SI Appendix*, Fig. S9).

We demonstrated the simultaneous multipoint intracellular action potential recording using OECT matrix. OECTs were placed at a pitch of 2 mm in a 4 × 4 matrix configuration. The channel size of 5 × 5 μm^2 and drain voltage of −600 mV were chosen to maximize the amplitude of recorded signals. Fig. 5*A* presents the matrix and cultured cardiomyocytes. The density of cells was different at each data point because of the relatively large cultured area (Fig. 5 *A*, *i* and *ii*). The baseline current of each pixel was about 200 to 300 μA (Fig. 5*B*). This indicates that they were capable of recording peaks after ∼15 d of cultivation. The matrix successfully recorded intracellular action potentials at multiple points with a sampling frequency of 2 kHz, as shown in Fig. 5*C*. Some points [such as (B-3)] recorded a clear electroporation-induced signal, and its amplitude reached 11 mV. Owing to the large amplitude, signals were clearly observed with relatively simple readout equipment. The SD of noise voltage was 140 μV, and the SNR at this data point was 37.9 dB. At some points such as (C-3), the recorded signal appears to be an incomplete electroporation-induced signal, which contains both the field potential and the intracellular action potential of small amplitude. The same data are displayed with a longer time window (47 s) in *SI Appendix*, Fig. S10. Although most OECTs continued recording successfully, the amplitude of the peaks attenuated after 30 s at

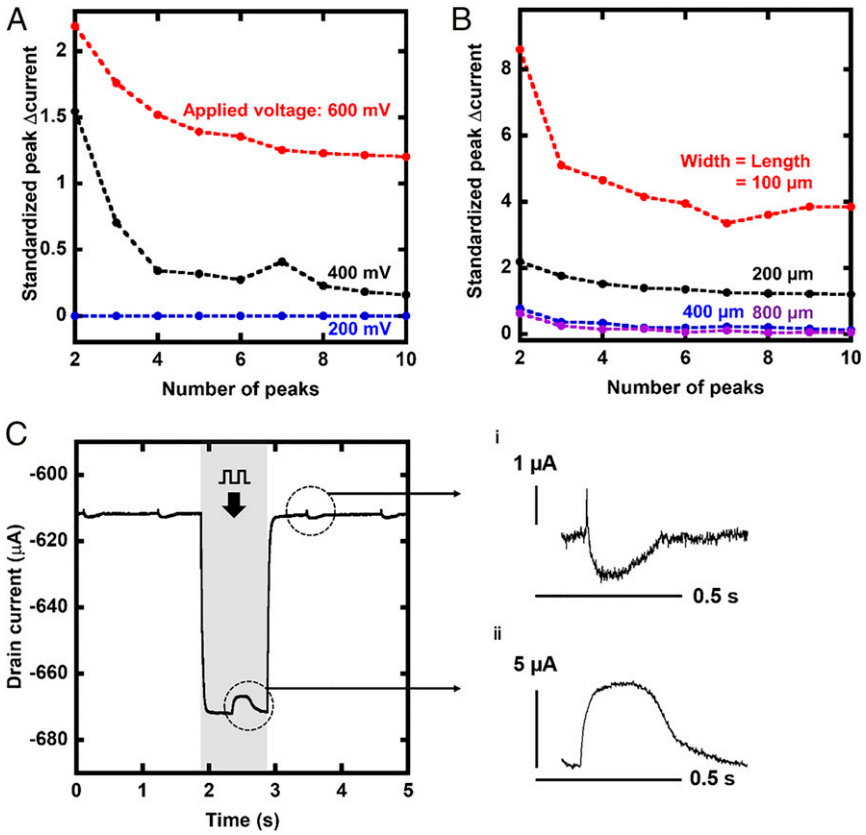

Fig. 4. Effect of recording conditions on the amplitude and duration of recorded intracellular action potential. (*A*) Amplitudes of intracellular action potentials induced by various pulse and drain voltages and their decay after the pulse. Larger voltage resulted in larger and longer intracellular action potentials recorded. The number of peaks were counted from the end of the pulse input, and the first peak was ignored to omit the effect of the drastic change of the baseline. The amplitude was standardized by that of a field potential before the stimulation. (*B*) Effect of scaling the channel size of the OECTs. An OECT with a small channel resulted in a large amplitude of recorded intracellular action potential and long duration by the recovery. (*C*) Signals recorded with the drain and pulse voltage of 200-mV amplitude and magnified peaks (*i* and *ii*). These were plotted using the data of Fig. 3*B*. The original data (10 kHz) was down-converted to 1 kHz to extract the signal overlapped with the pulse. The peak recorded during the pulse input had the features of intracellular potentials, although the first peak after the pulse input was the field potential, as it was recorded before the pulse input.

(B-2) and (B-4). This indicated that the continuous application of a 600-mV pulse potentially damaged the cells. The time delay of action potential is visualized in the heat map of *SI Appendix*, Fig. S11. The potentials were activated from (D-4) to (B-2). The time to travel from an edge pixel to another edge pixel (~4 mm) was about 40 to 60 ms, and the estimated propagation speed was roughly 80 μm/ms.

Discussion and Conclusion

In this study, we demonstrated intracellular action potential recording using OECTs and mapping with the matrix by operating it with an optimized configuration to induce electroporation during recording. The majority of organic transistors have a low career mobility. Thus, a larger width/length ratio is required to achieve a high g_m and high current. This can limit the realistic sensor density, even with the use of an interdigitated electrode (8, 28). Especially in the case of electroporation, an electrode with a larger admittance per area is preferred for applying a large electrical field in a small area. The PEDOT:PSS channel demonstrated a sufficient gate-drain current (>0.1 mA in 25 × 25 μm^2), and the intracellular action potential was successfully recorded.

The maximum amplitude of the recorded peaks was 93 μA, which corresponded to ~46 mV. This value was smaller than that of the patch-clamp and penetrating probe (~100 mV) but larger than that of the majority of previous studies using electroporation (<10 mV) (18, 23, 25). Unlike nanopillar/nanowire structures, OECTs have multiple cells on the channel. Therefore, the electroporation-induced peaks sometimes overlapped with the field potentials. By recording the signal during the application of the pulse, the amplitude of the electroporation-induced peaks was maximized and became >40 times larger than that of the field potentials without applying a larger voltage. In addition, the OECT matrix requires a relatively low voltage for electroporation. The threshold amplitude of the pulse for observing the effect of electroporation was only ~400 mV in our experiment; however, for other studies, particularly for those using a planar interface, values larger than 2 V have been reported (25, 26). Pillar/nanowire structures have been used to apply a larger electrical field in a small, well-sealed area of the cell membrane (29). The OECT does not have any specific three-dimensional structure, but its admittance per area increases in proportion to the thickness (11, 30, 31). Therefore, a PEDOT:PSS film of larger thickness has a lower impedance per area that is similar to a high-aspect-ratio pillar.

In the matrix configuration, the size of the channel was minimized to 5 × 5 μm^2, which is compatible with the scale of a single cardiomyocyte, and the matrix successfully recorded intracellular action potentials at multiple points. Unlike active matrices using organic transistors which have limited scan speed due to the slow response to gate bias (32), the drain current of the demonstrated OECT matrix is turned on immediately after the drain voltage is

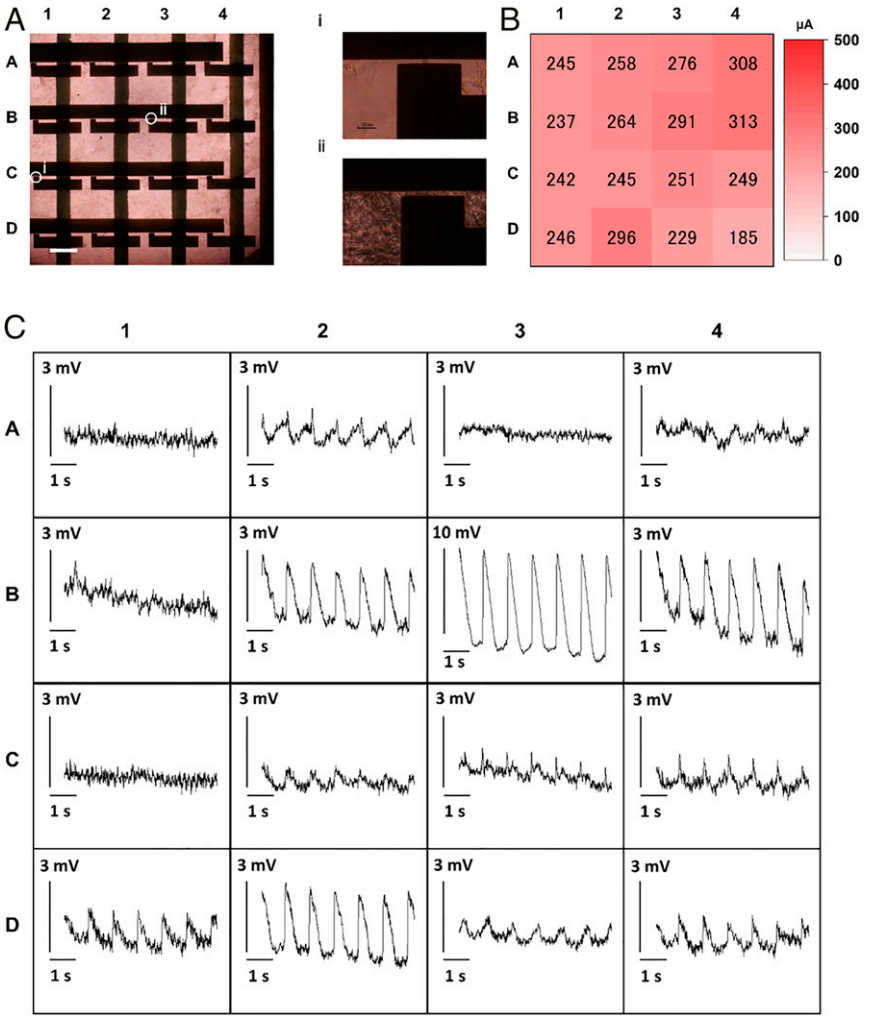

Fig. 5. Multipoint action potential recording using an OECT matrix. (*A*) Image of a matrix and hiPSC cardiomyocytes on it. It was prepared by merging multiple microscopic images. (Scale bar, 1 mm.) (*i* and *ii*) Enlarged images of the pixels at cell-poor region (*i*) and cell-rich region (*ii*). (Scale bar, 30 μm.) (*B*) Distribution of the base current of each pixel in the matrix. (*C*) The 4 × 4 action potential mapping. All images are plotted with the scale bar of 3 mV except in the case of B-3. Some points recorded the clear intracellular action potentials. Others recorded no signal or signals that were similar to the extracellular field potential.

applied. The response was faster than the recording cycle of the analyzer (50 μs). Thus, this method seems to be applicable to the high-speed scan of the larger matrix (1 kHz, 20 × 20 or more pixels), as long as no other issues such as crosstalk emerge. Six OECTs out of 16 (37%) recorded clear electroporation-induced signals with features, such as sharp rise and longer action potential duration, while another six recorded field potentials or incomplete electroporation-induced peaks. This result is not in the best category compared to the success rate previous reports have shown (30 to 90%) (23, 25, 33). The drain current of the miniaturized OECTs for the matrix (~250 μA) was smaller than that of OECTs for single-point recordings (~750 μA). Those facts indicate that the increased series resistance (>1 kΩ), which can be attributed to the contact resistance between Au and PEDOT:PSS (34), suppressed the actual current applied to the cells. Currently, the overlap length is designed to be 20 μm to ensure the contact, and thus it practically restricts the density of array at a pitch of ~100 μm, although the recording area itself is much smaller. Therefore, the reduction of the contact resistance using a chemical treatment, optimized geometry, and/or additional carrier injection layer (12, 34, 35) is crucial to realize the single-cell resolution in the future. These techniques are also important for low-voltage operation, which suppresses both the degradation of devices and damage to cells. In addition, advancement in external electronics such as multichannel current analyzer and crosstalk analysis are also important for implementation in the practical environment.

The aforementioned comparisons with existing methods are summarized in *SI Appendix*, Table S2. Whereas most of the other methods take advantage of complementary metal–oxide semiconductor compatibility, the OECT matrix offers a simple system fabricated via a mild process so that it is suitable for shape-adaptive or disposable applications using organic materials. It should be noted that each of the studies cited here should be carefully compared because they comprised different experimental conditions, such as the duration and the rise time of the applied pulse and the type of cells used. The definition of successful intracellular access is also different in each study.

The OECT matrix offers a scalable intracellular action potential recording system that is compatible with flexible organic electronic platforms. Although OECT-based systems are simple and compact, they have been often connected to special equipment for electrophysiology. Their combination with electroporation significantly improves the amplitude and quality of the original signal

applied to the OECTs and helps extract meaningful data using simple external equipment. This simple organic transistor platform could possibly lead to the future development of in vitro/vivo electrophysiology.

Materials and Methods

Materials and Fabrication Process of OECT. The details of the device structure and fabrication processes of the OECT are presented in *SI Appendix*, Fig. S12. First, a 5-nm-thick Cr and 75-nm-thick Au were thermally evaporated on a glass substrate. This layer was patterned by a liftoff process using a photoresist (ZEON Co. ZPN-1150). An 800-nm-thick parylene (diX-SR, KISCO Ltd.) layer was coated on the entire surface by a chemical vapor deposition process using SCS Labcoater, and holes were created on each drain electrode by an O_2 reactive ion etching process. The second Au layer was patterned for data line, which was connected to the drain electrode via the hole. As a passivation and sacrificial layer for the patterning of the channel, parylene/fluorinated polymer (1:6 mixture of 3M's Novec 1700 and 7100, spin-coated at 2,000 rpm)/parylene layers were subsequently deposited. The channel parts, including source-drain electrodes, were then selectively exposed by a reactive ion etching with a patterned photoresist to protect the other part. After the PEDOT:PSS solution was spin-coated and annealed at 100 °C, we peeled it off with the sacrificial layer, so that only the channel part was coated by PEDOT:PSS. It was then cross-linked by annealing at 140 °C for 2 h. The PEDOT:PSS solution used in this study comprised a mixture of 93.9 vol% aqueous dispersion (Clevios PH 1000 Heraus), 5 vol% ethylene glycol, 1 vol% (3-glycidyloxypropyl)trimethoxysilane, and 0.1 vol% dodecyl benzene sulfonic acid.

Characterization of OECT. The electrical performance of OECTs was measured using medium 199 as the electrolyte and an Ag/AgCl wire for applying a gate bias. The g_m curve and transient time responses to the pulse input were measured using a semiconductor parameter analyzer (B1500, Keysight). To record the output against the sine-wave input, which is presented in Fig. 2 *C* and *D*, we used a current waveform analyzer (CX3324A, Keysight). A waveform generator (33600A, Keysight) was used to supply both the driving voltage and the sine-wave input. The impedance sweep of the PEDOT:PSS electrode was measured using an LCR meter (E4980AL, Keysight). By assuming that an OECT works as a PEDOT:PSS electrode when shorting the source and drain electrode, we compared the performance of an OECT and a PEDOT:PSS electrode (*SI Appendix*, Fig. S13).

In Vitro Electrophysiology. hiPSC lines (201B7) were purchased from RIKEN (36). The cardiac differentiation protocol of hiPSCs expressing the α-MHC promoter and rex-1 promoter-driven drug-resistance genes in the bioreactor system (ABLE Co.) has been described previously (37). The hiPSC-derived cardiomyocytes were purified by puromycin treatment according to previous reports (7, 38). To culture the cells on an OECT matrix, we mounted a 12- × 12-mm^2 silicone frame on it and filled it with a solution for the dip-coating of fibronectin at a concentration of 6.25 $\mu g/cm^2$. Then, we seeded the purified hiPSC-derived cardiomyocytes (density: 3×10^5 cells/cm^2, day 20 from cardiac differentiation) on the day after the puromycin treatment and cultured them in an incubator (37 °C) with 5% CO_2 for at least 10 d. They were cultivated for 4 d because further cultivation makes the disassembly difficult. The samples were moved into another temperature-controlled chamber (37 °C) with an ambient gas composition before performing the recording, and the medium was replaced with Medium 199 Hanks' salts (12350039, Thermo Fisher Scientific) containing 10% fetal bovine serum and penicillin-streptomycin. While recording, the PEDOT:PSS/Au reference electrode was inserted into the medium instead of Ag/AgCl to avoid the effect of its toxicity. For single-point measurements, a waveform analyzer and waveform generator were used for high-definition recording and a well-controlled DC-Pulse pattern supply. For multipoint measurements, a custom-made circuit was used for driving the matrix. The details of the custom-made circuit have been described in previous studies (14, 39). According to the density of seeding, 30 cells are placed on a sample with the area of 100 × 100 μm^2. For much smaller samples, it is expected that the results are affected by the individuality and the number of cells on each sensor. Therefore, for the systematic experiment shown in Figs. 3 and 4, the smallest size was fixed at 100 μm.

Signal Processing and Data Analysis. The waveforms presented in Fig. 2 were processed by a low-pass filter. The threshold frequency was 1 kHz for 10-Hz input and 100 kHz for 1-kHz input. The action potentials recorded by the waveform analyzer were filtered by a low-pass filter (1 MHz), and in the case of Fig. 4*C*, 1 data point out of 10 data points was extracted to ignore the signal while the drain-source voltage was 0. The data presented in Fig. 5 is generated by multiple data processing: a 100-Hz low-pass filter, 45- to 55-Hz band-block filter, smoothing with an integration time of 10 ms, the removal of baseline shift using the exponential fitting, baseline cut, and conversion of current to voltage assuming a g_m of 1 mS for all pixels. It should be noted that the rising time of potentials is possibly overestimated by those processes. The SNR was calculated using the equation $SNR = 20 \log_{10} (A_{signal}/A_{noise})$, where A_{signal} is the scale of the recorded peak and A_{noise} is the SD of the noise from the baseline current. For Fig. 4 *A* and *B*, data required to plot a trend in a graph are obtained from a single substrate to minimize the effect of batch-to-batch distribution.

Image Editing. The brightness of the images in Fig. 5 *A*, *i* and *ii* is +20% of that of the original images.

Data Availability. All study data are included in the article and/or *SI Appendix*.

ACKNOWLEDGMENTS. This work was supported by Japan Society for the Promotion of Science (JSPS) Grant-in-Aid for Scientific Research (Grant 17H06149). Y.J. is supported by the Materials Education program for the future leaders in Research, Industry, and Technology. We acknowledge the technical assistance of Mitsuyoshi Shimane and Nanion Technologies Japan K.K.. We thank Itsuro Saito, Masaya Nishinaka, and Chihiro Okutani for technical support and fruitful discussions.

1. T. Someya *et al.*, Conformable, flexible, large-area networks of pressure and thermal sensors with organic transistor active matrixes. *Proc. Natl. Acad. Sci. U.S.A.* **102**, 12321–12325 (2005).
2. S. Wang *et al.*, Skin electronics from scalable fabrication of an intrinsically stretchable transistor array. *Nature* **555**, 83–88 (2018).
3. R. Feiner *et al.*, Engineered hybrid cardiac patches with multifunctional electronics for online monitoring and regulation of tissue function. *Nat. Mater.* **15**, 679–685 (2016).
4. J. Rivnay, H. Wang, L. Fenno, K. Deisseroth, G. G. Malliaras, Next-generation probes, particles, and proteins for neural interfacing. *Sci. Adv.* **3**, e1601649 (2017).
5. X. Dai, W. Zhou, T. Gao, J. Liu, C. M. Lieber, Three-dimensional mapping and regulation of action potential propagation in nanoelectronics-innervated tissues. *Nat. Nanotechnol.* **11**, 776–782 (2016).
6. T. Ohya *et al.*, Simple action potential measurement of cardiac cell sheet utilizing electronic sheet. *Artif. Life Robot.* **0**, 1–7 (2018).
7. S. Lee *et al.*, Ultrasoft electronics to monitor dynamically pulsing cardiomyocytes. *Nat. Nanotechnol.* **14**, 156–160 (2019).
8. T. Cramer *et al.*, Organic ultra-thin film transistors with a liquid gate for extracellular stimulation and recording of electric activity of stem cell-derived neuronal networks. *Phys. Chem. Chem. Phys.* **15**, 3897–3905 (2013).
9. V. Benfenati *et al.*, A transparent organic transistor structure for bidirectional stimulation and recording of primary neurons. *Nat. Mater.* **12**, 672–680 (2013).
10. D. Khodagholy *et al.*, High transconductance organic electrochemical transistors. *Nat. Commun.* **4**, 2133 (2013).
11. J. Rivnay *et al.*, High-performance transistors for bioelectronics through tuning of channel thickness. *Sci. Adv.* **1**, e1400251 (2015).
12. Y. Liang *et al.*, Tuning channel architecture of interdigitated organic electrochemical transistors for recording the action potentials of electrogenic cells. *Adv. Funct. Mater.* **29**, 1–10 (2019).
13. C. Yao, Q. Li, J. Guo, F. Yan, I.-M. Hsing, Rigid and flexible organic electrochemical transistor arrays for monitoring action potentials from electrogenic cells. *Adv. Healthc. Mater.* **4**, 528–533 (2015).
14. W. Lee *et al.*, Nonthrombogenic, stretchable, active multielectrode array for electroanatomical mapping. *Sci. Adv.* **4**, eaau2426 (2018).
15. X. Gu, C. Yao, Y. Liu, I. M. Hsing, 16-channel organic electrochemical transistor array for in vitro conduction mapping of cardiac action potential. *Adv. Healthc. Mater.* **5**, 2345–2351 (2016).
16. X. Gu *et al.*, Organic electrochemical transistor arrays for in vitro electrophysiology monitoring of 2D and 3D cardiac tissues. *Adv. Biosyst.* **3**, e1800248 (2019).
17. B. Tian, *et al.*, Three-dimensional, flexible nanoscale field-effect transistors as localized bioprobes. *Science* **329**, 830–834 (2010).
18. C. Xie, Z. Lin, L. Hanson, Y. Cui, B. Cui, Intracellular recording of action potentials by nanopillar electroporation. *Nat. Nanotechnol.* **7**, 185–190 (2012).
19. O. Caspi *et al.*, In vitro electrophysiological drug testing using human embryonic stem cell derived cardiomyocytes. *Stem Cells Dev.* **18**, 161–172 (2009).
20. J. Abbott *et al.*, A nanoelectrode array for obtaining intracellular recordings from thousands of connected neurons. *Nat. Biomed. Eng.* **4**, 232–241 (2020).
21. O. P. Hamill, A. Marty, E. Neher, B. Sakmann, F. J. Sigworth, Improved patch-clamp techniques for high-resolution current recording from cells and cell-free membrane patches. *Pflugers Arch.* **391**, 85–100 (1981).
22. Q. Qing *et al.*, Free-standing kinked nanowire transistor probes for targeted intracellular recording in three dimensions. *Nat. Nanotechnol.* **9**, 142–147 (2014).

23. J. Abbott *et al*., CMOS nanoelectrode array for all-electrical intracellular electrophysiological imaging. *Nat. Nanotechnol.* **12**, 460–466 (2017).
24. B. X. E. Desbiolles, E. de Coulon, A. Bertsch, S. Rohr, P. Renaud, Intracellular recording of cardiomyocyte action potentials with nanopatterned volcano-shaped microelectrode arrays. *Nano Lett.* **19**, 6173–6181 (2019).
25. D. Braeken *et al*., Open-cell recording of action potentials using active electrode arrays. *Lab Chip* **12**, 4397–4402 (2012).
26. H. B. Hayes *et al*., Novel method for action potential measurements from intact cardiac monolayers with multiwell microelectrode array technology. *Sci. Rep.* **9**, 11893 (2019).
27. D. Khodagholy *et al*., In vivo recordings of brain activity using organic transistors. *Nat. Commun.* **4**, 1575 (2013).
28. W. Lee *et al*., Integration of organic electrochemical and field-effect transistors for ultraflexible, high temporal resolution electrophysiology arrays. *Adv. Mater.* **28**, 9722–9728 (2016).
29. J. Abbott, T. Ye, D. Ham, H. Park, Optimizing nanoelectrode arrays for scalable intracellular electrophysiology. *Acc. Chem. Res.* **51**, 600–608 (2018).
30. A. V. Volkov *et al*., Understanding the capacitance of PEDOT:PSS. *Adv. Funct. Mater.* **27**, 1700329 (2017).
31. A. Williamson *et al*., Localized neuron stimulation with organic electrochemical transistors on delaminating depth probes. *Adv. Mater.* **27**, 4405–4410 (2015).
32. T. Someya *et al*., A large-area, flexible pressure sensor matrix with organic field-effect transistors for artificial skin applications. *Proc. Natl. Acad. Sci. U.S.A.* **101**, 9966–9970 (2004).
33. M. Dipalo *et al*., Plasmonic meta-electrodes allow intracellular recordings at network level on high-density CMOS-multi-electrode arrays. *Nat. Nanotechnol.* **13**, 965–971 (2018).
34. S. M. Kim *et al*., Influence of PEDOT:PSS crystallinity and composition on electrochemical transistor performance and long-term stability. *Nat. Commun.* **9**, 3858 (2018).
35. M. Zabihipour *et al*., High yield manufacturing of fully screen-printed organic electrochemical transistors. *npj Flex. Electron.* **4**, 15 (2020).
36. K. Takahashi *et al*., Induction of pluripotent stem cells from adult human fibroblasts by defined factors. *Cell* **131**, 861–872 (2007).
37. K. Matsuura *et al*., TRPV-1-mediated elimination of residual iPS cells in bioengineered cardiac cell sheet tissues. *Sci. Rep.* **6**, 21747 (2016).
38. D. Sasaki *et al*., Contractile force measurement of human induced pluripotent stem cell-derived cardiac cell sheet-tissue. *PLoS One* **13**, e0198026 (2018).
39. W. Lee *et al*., Transparent, conformable, active multielectrode array using organic electrochemical transistors. *Proc. Natl. Acad. Sci. U.S.A.* **114**, 10554–10559 (2017).